ECS Transactions, 78 (1) 1011-1020 (2017)
10.1149/07801.1011ecst ©The Electrochemical Society

Study of the Mechanisms of O_2-Reduction and Degradation Operating on $La_{0.5-X}Pr_xBa_{0.5}CoO_{3-\delta}$ Cathodes for SOFCs

D. Garcés[a], H. Wang[b], S. A. Barnett[b], A. G. Leyva[a,c], L. V. Mogni[d]

[a] CNEA, Centro Atómico Constituyentes, San Martin B1650KNA, Argentina
[b] Northwestern University, Department of Materials Science and Engineering Evanston, Illinois 60208, USA
[c] ECyT-UNSAM, San Martin B1650KNA, Argentina
[d] CONICET/CNEA, Centro Atómico Bariloche, S. C. de Bariloche 8400, Argentina

The oxygen reduction mechanism and time evolution behavior were studied for porous $La_{0.5-x}Pr_xBa_{0.5}CoO_{3-\delta}$ (LPBC) electrodes deposited onto $Ce_{0.9}Gd_{0.1}O_{1.95}$ electrolytes. Electrochemical impedance spectroscopy (EIS) measurements, performed between 400 and 800°C as a function of pO_2, show that the electrochemical response is limited by O_2-gas diffusion and surface reaction (O-surface exchange + O-ion diffusion). The time evolution of the cathode resistance at 700°C in air shows an increase from 0.03 to 0.05 Ωcm^2 after 280 h of testing. Three-dimensional (3D) tomographic using focused ion beam–scanning electron microscopy (FIB-SEM) showed little changes of microstructure after the ageing. The increase in resistance was explained by an increase in the amount of a water-soluble Ba-rich surface phase by a factor of 2, after ageing of the LPBC electrode, by an etching procedure coupled with inductively coupled plasma-optical emission spectrometry (ICP-OES).

Introduction

The large-scale commercialization of SOFCs is currently constrained by a combination of cost and durability issues. In order to address these concerns, much effort has been focused on developing low-temperature SOFCs (LT-SOFCs), with cell operating temperature < 700°C (1). One of the major issues to achieve this goal is the development of cathode materials with low polarization resistance and good stability over time.

Cobaltites with the perovskite structure such as, the strontium barium cobaltite $Ba_{0.5}Sr_{0.5}Co_{0.8}Fe_{0.2}O_{3-\delta}$ (BSCF) (2) are promising cathode materials for LT-SOFCs. Despite the good performance of Sr-containing perovskites, one major issue is the long-term instability due to Sr-surface segregation (3). Yildiz group pointed out, from the study of thin film electrodes, that the cation surface segregation increases due to the size mismatch between the dopant and host cations, being more important the Ba surface segregation than Sr and Ca surface enrichment for $(La,M)MnO_3$ with M = Ba, Sr or Ca electrodes (4). However, there is not enough information about Ba-segregation issue in Ba-cobaltites porous electrodes. In these perovskites, the Ba plays a key role since its large cation radii mismatch also distorts the cubic crystal structure promoting the oxygen vacancy formation and migration (5) reducing the $R_{c,p}$ due to the improvement of the O-

surface exchange and the O-ion diffusion. However, the same structural distortion, also induces a slow segregation of a hexagonal perovskite phase (6-8) which deteriorates the O_2 reduction kinetics with time (9). Recent work has shown that $La_{0.5}Ba_{0.5}CoO_{3-\delta}$ is a promising cathode material for LT-SOFCs because of its low cathode polarization resistance (10-12). Besides, in this oxide we did not observe the hexagonal phase formation suggesting that La^{+3} ions play an important role stabilizing the cubic phase because of its charge and ionic radii.

With these ideas, in this work, the La content of the perovskite oxide $La_{0.5}Ba_{0.5}CoO_{3-\delta}$ is partially substituted with Praseodymium as $La_{0.5-x}Pr_xBa_{0.5}CoO_{3-\delta}$ (LPBC), with $0 < x < 0.5$ with the aim to improve even more the cathode performance. Samples exhibit cubic symmetry for $x \leq 0.35$, whereas above this value the cation ordering produces a layering structure with tetragonal symmetry. The Electrochemical Impedance Spectroscopy (EIS) as a function of temperature (T), oxygen partial pressure (pO_2) and time in combination with 3D focused ion beam-scanning electron microscopy (FIB-SEM) tomography and the inductively coupled plasma-optical emission spectrometry (ICP-OES) studies were used to analyze the mechanism of O_2 reduction and the origin of degradation with time.

Experimental

Powders with nominal composition $La_{0.5-x}Pr_xBa_{0.5}CoO_{3-\delta}$ were synthesized via a combined EDTA-citrate complexing sol-gel process. Stoichiometric amounts of $La(NO_3)_3 \cdot 6H_2O$, $Ba(NO_3)_2$, $Co(NO_3)_3 \cdot 6H_2O$ and $Pr(NO_3)_2 \cdot xH_2O$ were dissolved into EDTA-$NH_3 \cdot H_2O$ solution (pH ≈ 6) under heating and stirring. A proper amount of citric acid-$NH_3 \cdot H_2O$ solution (pH ≈ 6) was added at a mole ratio of 1:1:2 for EDTA: total metal ions: citric acid. The mixed solution was firstly evaporated at 80ºC to form a red transparent gel and then heated at 150ºC for several hours to obtain a dark dry foam structure. After decomposed on a hot plate, the powders were calcined at 400ºC (4 h, in air) and then at 1000ºC (4 h, in air). Each sample of the LPBC series was labeled according to its corresponding lanthanum content, i.e., La30 represents the $La_{0.30}Pr_{0.20}Ba_{0.50}CoO_{3-\delta}$ compound.

The absence of secondary phases was verified by X-ray diffraction (XRD) by using a PANalytical Empyream with a PIXcell 3D detector employing Cu-Kα radiation.

The cells consist of a dense $Ce_{0.9}Gd_{0.1}O_{1.95}$ (GDC, Fuel Cell Materials) electrolyte (area ~0.8 cm^2, thickness ~0.1 cm), where a porous layer of GDC and a porous layer of LPBC were deposited by spin coating. The inks were prepared by mixing the corresponding ceramic powders (GDC or LPBC) with ethanol, α-terpineol (≥ 96%, Sigma Aldrich), polyvinyl butyral (Sigma Aldrich), and polyvinyl pyrrolidone (Sigma Aldrich) in a 40:40:27:2:1 mass ratio. The porous layer of GDC improves the adherence of LPBC cathode onto the GDC dense electrolyte (13). After deposition, the porous GDC layer was heat treated at 1400 ºC during 1 h in air, while the LPBC porous electrode was heat treated at 1000ºC 1 h in air.

The electrode microstructures were characterized by Field Emission Gun Scanning Electron Microscopy (FEG-SEM) with a FEI Nova NANO 230 microscope. The

electrode thicknesses are analysis by fracturing, epoxy infiltration and polishing. Serial sectioning was done on a FEI Helios. Backscattered electron (BSE) detector with an accelerating voltage of 2 kV was used to obtain good contrast between solid and pore phases. Microstructural parameters including porosity, tortuosity, surface area and particle size distribution were then calculated based on the 3D data.

ICP-OES analysis was also done using a Thermo Scientific iCAP 7600 spectrometer on the fresh and post-tested samples to examine possible changes in the cation surface segregation. The samples were fractured into three fragments and stirred in ultrapure H_2O for 10 min, followed by transferring the samples into a 12 mol·L^{-1}HCl solution and stirring until the electrodes were completely dissolved. The ultrapure H_2O and the concentrated HCl solutions were mixed with the appropriate amounts of H_2O/HCl/HNO_3 to yield 0.36 mol·L^{-1}HCl/0.72 mol·L^{-1} HNO_3 solutions for ICP-OES injection. A certified stock solution (10.00 µg/mL from Inorganic Ventures) containing La, Pr, Ba and Co was used to prepare the calibration standards for quantification. The following background corrected emission lines were chosen for evaluation: La (379.478 nm; 412.323 nm), Pr (414.311 nm; 417.939 nm; 422.535 nm), Ba (233.527 nm; 455.403 nm; 493.409 nm), Co (228.616 nm; 237.862 nm).

The electrochemical performance was evaluated by Electrochemical Impedance Spectroscopy (EIS) on symmetrical cells configuration (LPBC/GDC/LPBC) by using an AUTOLAB PGSTAT30 (EcoChemie) potentiostat coupled to a FRA2 analyzer. The EIS measurements for La30 were carried out in air in a temperature range between 400 and 800ºC. At 600 and 700ºC the EIS spectra were collected varying the oxygen partial pressure (pO_2) between 1 and 5x10^{-4} atm by using a home-made device to test symmetrical cells coupled to an electrochemical oxygen pump and sensor. In addition, EIS spectra were also collected at 0.2 and 0.05 atm varying the temperature, with 50 ºC step, between 500 and 800ºC. Life testing was performed at 700ºC in air for La35 sample.

Results and Discussion

Structure and Microstructure Characterization

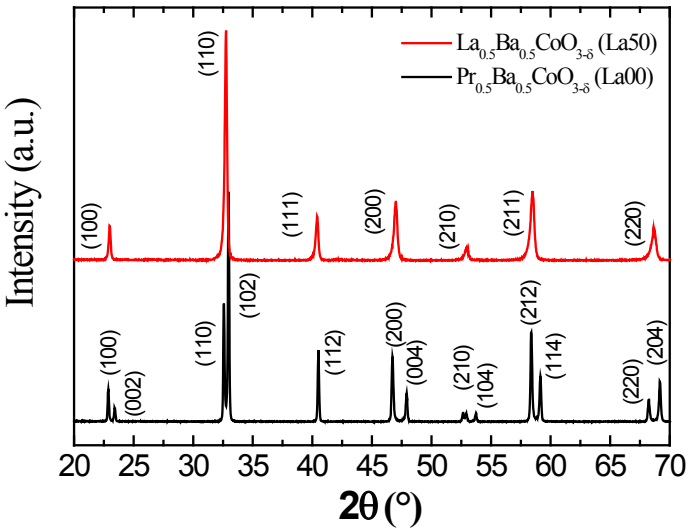

Figure 1. XRD pattern of La00 and La50 samples.

Figure 1 shows the XRD pattern of La50 and La00 sample where Bragg index of each peak was included in the graphic. The analysis of XRD data shows that above La content of 0.15 samples can be indexed as cubic perovskite (space group $Pm\bar{3}m$), otherwise a peak splitting indicates the formation of a tetragonal (space group $P4/mmm$) phase below La content of 0.15.

Figure 2.a) and 2.b) are SEM images showing cross sectional and electrode surface views of the symmetrical cell La35/CGO/La35, respectively. Figure 2.c) and 2.d) illustrates 2D FIB-SEM cross-sectional image of the La35-fresh and tested sample, respectively. The bright phase represents the particles and the dark phase is the epoxy-infiltrated pores. The corresponding 3D reconstructed structure of the La35-fresh and tested sample is shown in Figure 2.e) and 2.f). The structure is typical of SOFC cathode electrode produced by firing of particle compacts, showing reasonably uniform particle sizes and good necking between particles. Table I indicates the microstructural parameters, solid phase fraction (ε), solid phase and pore phase tortuosities (τ_s, τ_p), specific surface area (a) and the mean particle size determined from the analysis of the 3D data and the cumulative particle size distribution (Figure 2.g)) of La35 before and after life testing.

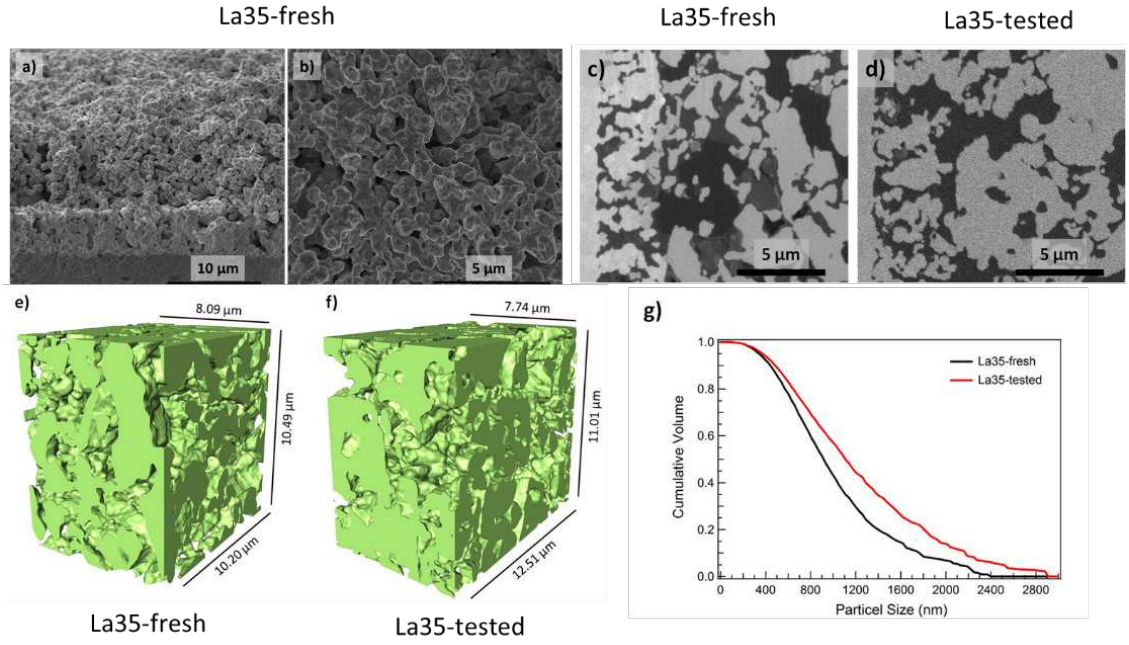

Figure 2. SEM images of La35 symmetrical cell, a) cross and b) top section. Typical 2D FIB-SEM cross-sectional image of c) La35-fresh and d) La35-tested with pore phase infiltrated by epoxy. The corresponding 3D reconstruction of e) La35-fresh and f) La35-tested with LPBC particles shown in green and pores transparent. Note that the 3D view only shows the electrode region. g) Cumulative particle size distribution of LPBC calculated from obtained 3D data sets.

TABLE I. Microstructural parameters for La35 sample

Sample	solid phase fraction (ε)	solid phase tortuosity (τ_s)	pore phase tortuosity (τ_p)	specific surface area (a)	mean particle size
La35 - fresh	52.4 %	1.28	1.22	3.78 μm^{-1}	900 nm
La35 - tested	53.7%	1.28	1.25	3.12 μm^{-1}	1100 nm

Electrochemical Characterization

Figures 3.b) and 3.c) show typical examples of impedance spectra, Nyquist and Bode plots (data points), measured at 600ºC and pO_2 = 0.05 atm for the symmetrical cell La30/GDC/La30 and Figures 3.d) and 3.e) show the same information at 700 ºC. All data collected were normalized to the geometric area of the electrodes in the symmetrical cell configuration. All spectra show two arcs denoting two different processes, one occurring at high frequency that is well-fit using a Gerischer-type element and the other occur at low frequency that is well-fit using a R//CPE element. Similar results were reported for Pr-free La-Ba cobaltite (10). The two arcs are observed at temperatures above 600°C, but only one EIS arc is observed at lower temperature. All cathode compositions present similar behavior shown in Figure 3.

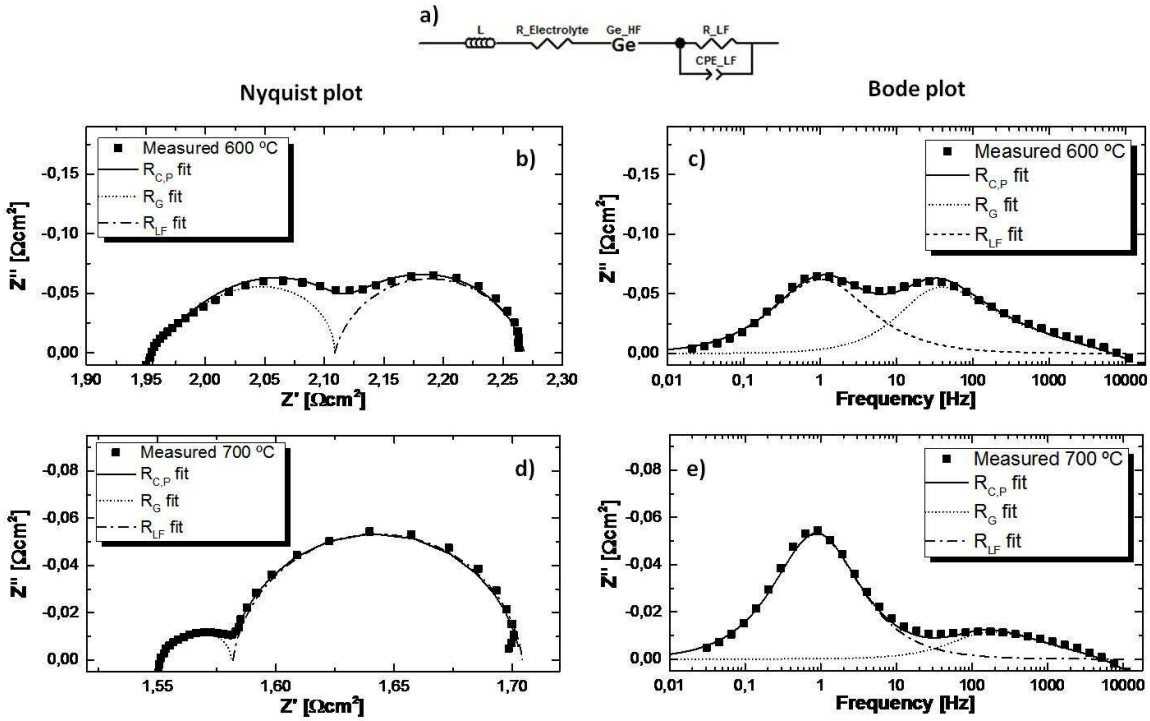

Figure 3. a) Equivalent circuit used for fitting the EIS spectra in the whole frequency range. b,d) Nyquist and c,e) Bode plot obtained for La30 sample in a pO_2 = 0.05 atm at 600 and 700ºC, respectively. Data point represents the measured data, solid line represent the arcs resulting of fitting data with equivalent circuit proposed and dashed lines indicating the different contributions.

Figure 4 shows the total polarization resistance evaluated at 600 and 700°C for all compositions. Regardless of the La content, $R_{C,P}$ takes values between 0.07 and 0.22 Ωcm^2 at 600°C and between 0.03 and 0.06 Ωcm^2 at 700°C.

In order to study the mechanism of the O_2 reduction reaction (ORR), the electrochemical response of the cubic La30 electrode was analyzed as a function of T and pO_2. The EIS spectra were fitted using the Electrical Equivalent Circuits (EEC) approximation. This circuit is composed by the inductance of connectors (L) and the electrolyte resistance (R_electrolyte), whereas the electrode response is fitted by the combination of a Gerischer for high frequency arc (HF) and a resistance (R_LF) in

parallel with a capacitor (Cpe_LF) for the low frequency arc (LF) (see Figure 3.a)).The resulting fits show good agreement with the measured spectrum.

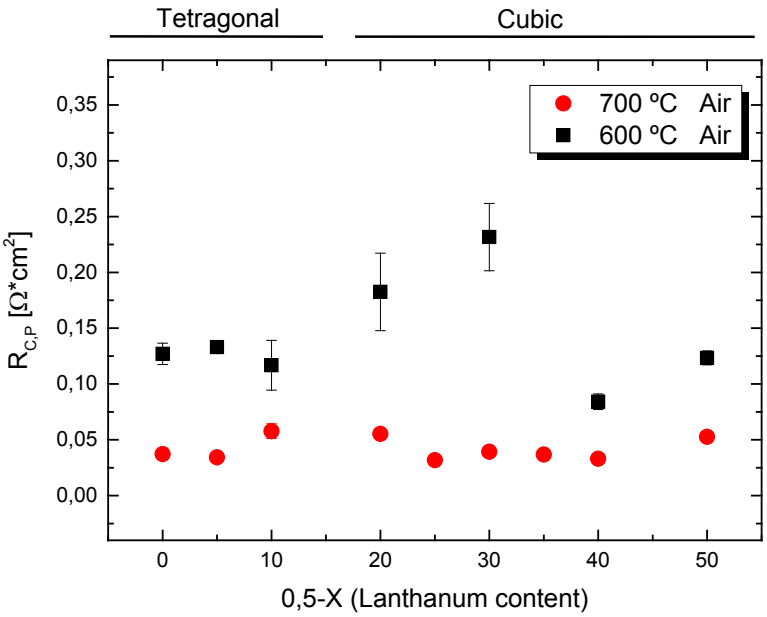

Figure 4. Total polarization resistance as function of lanthanum content at 600 and 700°C in air.

Figures 5.a) and 5.b) show the log-log plot for the high frequency Gerischer resistance (R_G) and the low frequency resistance (R_{LF}) vs pO_2 at 600 and 700°C for the La30 sample. The pO_2 dependences of R_G and R_{LF} fit approximately to $R_G \propto (pO_2)^{-0.25}$ and $R_{LF} \propto (pO_2)^{-1}$. Figure 5c) shows the Arrhenius plot of R_G and R_{LF} obtained from the fitting of EIS spectra collected as a function of T in air and $pO_2 = 0.05$ atm. Both process show markedly different activation energies. Whereas the R_G has an activation energy ~ 1 eV the O_2-gas diffusion is almost independent of T. These results suggest that the electrochemical response is limited by one or both of two mechanisms, depending on the conditions. At temperatures $\leq$ 600°C, the target T for low temperature SOFC (1), the high frequency contribution R_G associated with co-limiting O-surface exchange and O-bulk diffusion (14,15) is dominant. Whereas at higher temperatures (T > 700ºC) R_G becomes small enough, or at very low pO_2 the low frequency R_{LF} response increases being in both cases the O_2-gas diffusion the main responsible of the cathode polarization losses. A previous work in cathode with similar composition shown that the polarization resistance associated to O_2-gas diffusion takes similar values independently of microstructure for electrodes with significant differences in particle sizes (10). This result suggested that the O_2 gas transport limitation due to the gas diffusion is through the pores but also trough the layer boundary between the porous electrode and the gas phase.

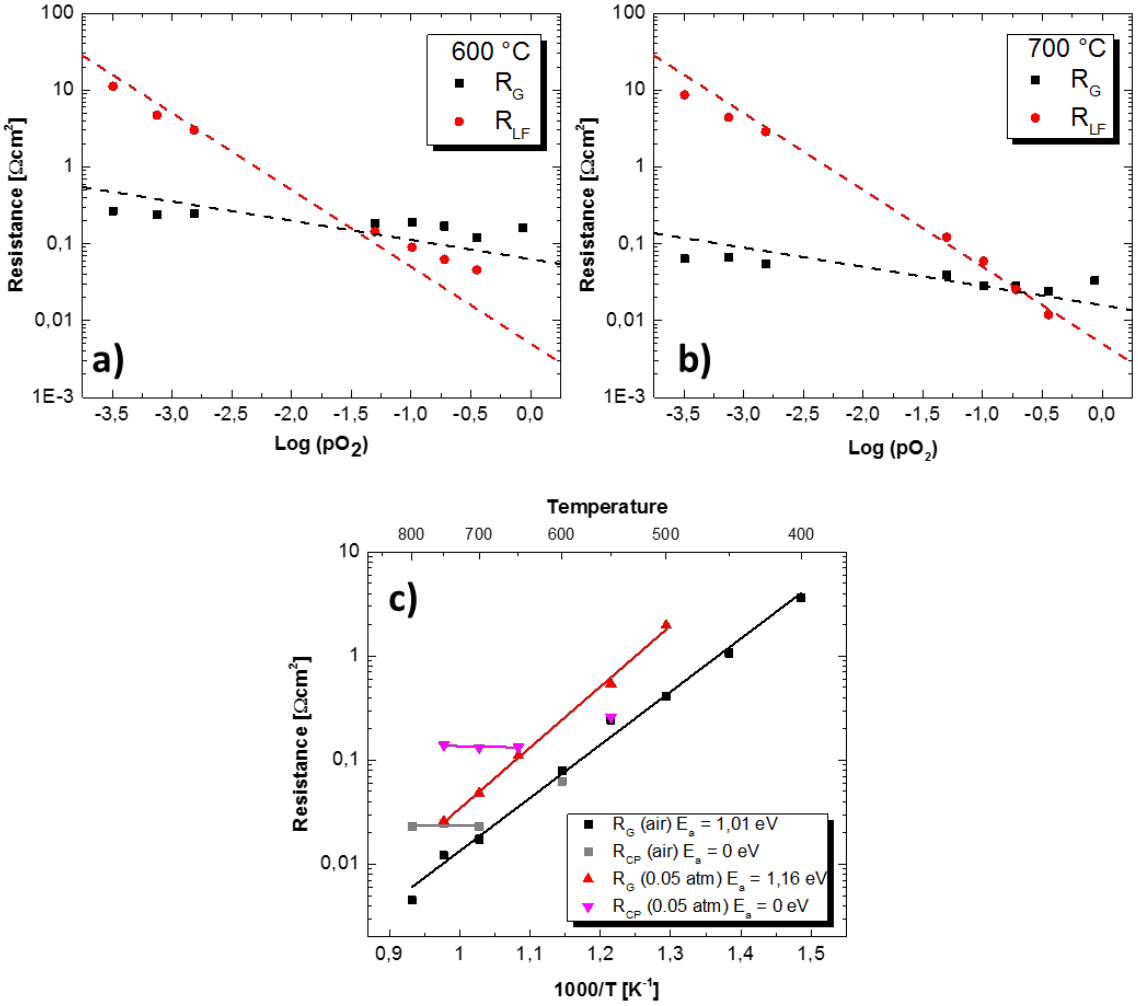

Figure 5. a) and b) Log-log plot of the high frequency Gerischer resistance (R_G) and the low frequency resistance (R_{LF}) with pO_2 at 600 and 700°C for La30 sample. Dotted lines indicate the pO_2 dependences $R_G \propto (pO_2)^{-0.25}$ and $R_{LF} \propto (pO_2)^{-1}$. b) Arrhenius plot for the Gerischer resistance (R_G) and the low frequency resistance (R_{LF}) in air and pO_2 = 0.05 atm. The activation energies are indicated on the graphs.

Life Testing

Figure 6 shows the time evolution of R_G and R_{LF}, measured by EIS at 700°C in air, and their sum, for the La35 electrode. The results reveal an increase of the total polarization resistance by ~ 67 % over 280 hours. The overall rate of change over this time, defined as $\frac{1}{R^0_{C,P}}\frac{dR_{C,P}}{dt}$, is 0.002 h^{-1}. As it can be observed from figure 6, the low frequency contribution (R_{LF}) is the major contribution to the polarization resistance, but it changes only ~ 20% at the end of the test ($\frac{1}{R^0_{LF}}\frac{dR_{LF}}{dt} = 0.0009\ h^{-1}$). Whereas the low frequency R_G triples its value ($\frac{1}{R^0_G}\frac{dR_G}{dt} = 0.009\ h^{-1}$, increasing ~ 200 %). The little increase of R_{LF} can be attributed to the particle coarsening reported in Table 1 which reduce the pore fraction ($\varepsilon_P = 1 - \varepsilon$) and increases the pore phase tortuosity (τ_p) - i.e. $R_{LF} \propto \frac{\tau_p}{\varepsilon_p}$ (14)

- whereas the increases of R_G cannot be totally explained by the reduction of the specific surface area - i.e. $R_G \propto \frac{1}{\sqrt{a}}$ (14).

The amount of Ba segregated on the electrode surfaces after the La35 life test was measured using ICP measurements of BaO preferentially solubilized in water, and compared with the as-prepared electrode. As shown in Figure 7, the amount of surface Ba is doubled, which can explain the increase of R_G during the life test. Comparing these results with previous works where the Sr-surface segregation was evaluated for $La_{0.6}Sr_{0.4}Co_{0.2}Fe_{0.8}O_{3-\delta}$ cathode (16), it can be conclude that the segregation of Ba produces a greater degradation of the cells. This conclusion is based not only to the increases of Ba surface concentration - i.e. Ba surface concentration is duplicated in the half of time that Sr concentration due it - but also for the larger cation surface concentration.

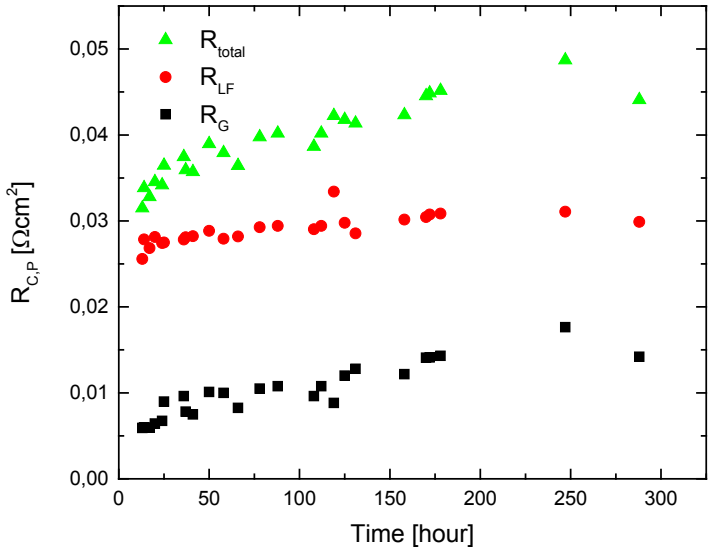

Figure 6. Evolution of $R_{C,P}$, R_G and R_{LF} values with aging time for La35 sample at 700°C in air.

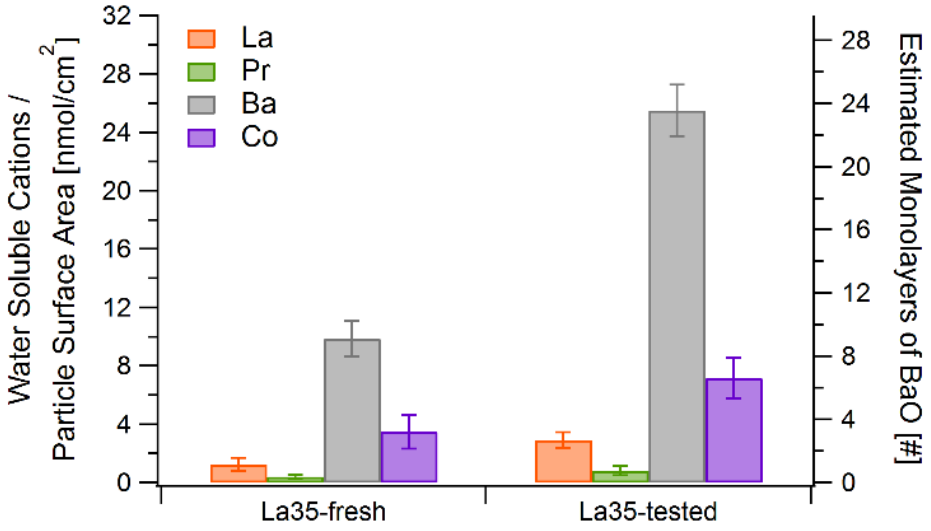

Figure 7. Amounts of water-soluble cations detected by ICP-OES. The cation amounts were normalized to LPBC surface area, obtained by 3D FIB-SEM as shown in Table I.

Conclusions

A soft chemical route was used to obtain $La_{0.5-x}Pr_xBa_{0.5}CoO_{3-\delta}$ powders. The study of electrode performance by EIS as a function of temperature, pO_2 and time suggested that two processes contribute to $R_{C,P}$:

1) The low frequency resistance (R_{LF}) that is associated to O_2 gas diffusion. This contribution dominates the cathode polarization resistance as T increases or pO_2 decreases. The O_2 gas transport resistance shows little changes with time which is in agreement with small change of microstructure.

2) The high frequency Gerischer-resistance (R_G) that is in agreement with the ALS approximation. This R_G considers that the O_2-reduction reaction is co-limited by O-surface exchange and O-bulk diffusion. This mechanism is mostly determined by the crystal structure, microstructure and surface conditions. The R_G is the contribution showing the largest evolution with time.

Ageing of La35 symmetric-electrode cells with GDC electrolytes, carried out at 700ºC for 280 hours in air, resulted in an increase of the electrode polarization resistance by about 67 %. 3D tomographic analysis indicated no significant microstructural changes due to ageing. ICP-OES measurements of selectively dissolved surface species show that the amount of surface Ba increased by ~ 2 times after the thermal ageing. Therefore, it is reasonable to conclude that Ba surface segregation, rather than microstructural changes, caused the increased La35 polarization resistance.

Acknowledgements

Authors want to acknowledge the support of CONICET-NSF collaborative project. Conventional XRD studies were performed at the X-ray Diffraction Laboratory, Department of the Condensed Matter Physics, GIyA, GAIyANN-CAC-CNEA. The authors also acknowledge the assistance of the Electron Probe Instrumentation Center (EPIC) at the NUANCE Center-Northwestern University, which has received support from the MRSEC program (NSF DMR-1121262) at the Materials Research Center; the International Institute for Nanotechnology (IIN); and the State of Illinois, through the IIN.Metal analysis was performed at the Northwestern University Quantitative Bio-element Imaging Center.

References

1. Gao, Z., Mogni, L.V., Miller, E. C., Railsback, J. G., Barnett, S. A. *Energy and Environmental Science*. **9** (5), 1602-1644 (2016).
2. S.M.H. Zongping Shao, *Nature,* **431**, 170–173 (2004).
3. S. P. Simner, M. D. Anderson, M. H. Engelhard, J. W. Stevenson, *Electrochemical and Solid-State Letters,* **9** (10), A478 (2006).
4. W. Lee, J. W. Han, Y. Chen, Z. Cai, and B. Yildiz. *J. Am. Chem. Soc*., **135**(21), 7909–7925 (2013).
5. R. Merkle, Y. Mastrikov, E. Kotomin, M. M. Kuklja, J. Maier, *J. Electrochem. Soc*. **159**, B219–B219 (2012).

6. D.N. Mueller, R.A. De Souza, T.E. Weirich, D. Roehrens, J. Mayer, M. Martin, *Phys. Chem. Chem. Phys*., **12,** 10320–10328 (2010).
7. K. W. Silvie Švarcova, J. Tolchard, H. J. M. Bouwmeester, T. Grande, *Solid State Ionics,* **178**, 1787–1791 (2008).
8. K. Efimov, Q. Xu, A. Feldhoff, *Chem. Mater*., **22**, 5866–5875 (2010).
9. S. Yakovlev, C. Y. Yoo, S. Fang, H.J.M. Bouwmeester, *Appl. Phys. Lett*., **96**, 254101–254101 (2010).
10. D. Garcés, A. L. Soldati, H. Troiani, A. Montenegro-Hernández, A. Caneiro, L. Mogni, *Electrochimica Acta,* **215**, 637–646 92016).
11. S. Pang, X. Jiang, X. Li, Z. Su, H. Xu, Q. Xu, C. Chen, *Int. J. Hydrogen Energy,* **37**, 6836-6843 (2012).
12. R. Amin, K. Karan. *J. Electrochem. Soc*., **157** (2010) B285–B285.
13. C. F. Setevich, L. V. Mogni, A. Caneiro, F.D. Prado, *Int. J. Hydrogen Energy*., **37**, 14895–14901 (2012).
14. S. B. Adler, J. A. Lane, B.C.H. Steele, *J. Electrochem. Soc*., **143**, 3554–3564 (1996).
15. Y. Lu, C. Kreller, S.B. Adler, *J. Electrochem. Soc*., **156**, B513–B513 (2009).
16. H. Wang, K. J. Yakal-Kremski, T. Yeh, G. M. Rupp, A. Limbeck, J. Fleig, and S. A. Barnett, *Journal of The Electrochemical Society*, **163** (6), F581-F585 (2016)